*J. Fluid Mech.* (2007), *vol.* 574, *pp.* 317–342.  
doi:10.1017/S0022112006004113 Printed in the United Kingdom

# Convection of a binary fluid saturating a shallow porous cavity subjected to cross heat fluxes

A. BAHLOUL[1], P. VASSEUR[2] AND L. ROBILLARD[2]

[1]Institut de Recherche Robert-Sauvé en Santé et Sécurité du Travail, 505, boul. de Maisonneuve Ouest, Montral, PQ H3A 3C2, Canada

[2]Department of Mechanical Engineering, Ecole Polytechnique, University of Montréal, C.P. 6079, Succ. 'Down-Town' Montréal, Québec, H3C 3A7, Canada

(Received 24 September 2005 and in revised form 12 September 2006)

In this work, natural convection in a differentially heated binary mixture is studied analytically and numerically. The fluid is subjected to the Soret effect and is contained in a shallow rectangular porous cavity. All four faces are exposed to uniform heat fluxes, opposite faces being heated and cooled, respectively. Analytical solutions for the stream function, temperature and concentration fields are obtained using a parallel flow assumption in the core region of the cavity and an integral form of the energy and constituent equations. Numerical confirmation of the analytical predictions is also obtained. Results are presented first in the presence of a vertical temperature gradient ($a=0$) for which the solution takes the form of a standard Bénard bifurcation. For this situation, steady bifurcations are either pitchfork or subcritical, depending on the separation parameter $\varphi$ and Lewis number $Le$. The imperfection brought by a horizontal temperature gradient ($a\neq 0$) to the bifurcation is then investigated. Both the nonlinear analytical model and the numerical solution indicate that, depending on $a$, $\varphi$ and $Le$, the onset of motion occurs through subcritical bifurcations. The existence of transcritical bifurcations is also demonstrated. The special case where the buoyancy forces induced by the thermal and solutal forces are opposing and of equal intensity ($\varphi=-1$) is also discussed. For this particular situation, the supercritical Rayleigh number for the onset of convection is predicted on the basis of a linear stability analysis. Multiple steady states near the threshold of convection are found.

## 1. Introduction

Recently, convection in a porous medium saturated by a binary fluid has received attention owing to its relevance in many natural and industrial problems. Prominent among these are the migration of moisture contained in fibrous insulation, grain storage, the transport of contaminants in saturated soils, the underground disposal of nuclear wastes, drying processes, etc. Convection in binary fluids is more complex than in pure fluids as a consequence of the difference in time-scale diffusion between energy and species. The concentration in binary fluids may be induced by the solutal boundary conditions applied on the system (double-diffusive problems). However, the species gradients can also be induced in a binary solution by the thermal gradients via the Soret effect (cross-diffusion problems).

Earlier works on double-diffusive natural convection in porous media are concerned with the case of a horizontal layer heated and salted from the bottom. For this configuration the onset of convection was predicted by Nield (1967), on the basis

of a linear stability analysis, for various thermal and solutal boundary conditions. This flow configuration was reconsidered by Taunton, Lightfoot & Green (1972), Rudraiah, Shrimani & Friedrich (1986) and Taslim & Narusaw (1986). A linear stability analysis was carried out by Poulikakos (1986) to study double diffusive convection in a horizontal sparsely packed porous layer. The flow in the porous matrix was investigated by using the Brinkman-extended Darcy model, which accounts for friction due to macroscopic shear. Results for a pure viscous fluid and a Darcy (densely packed) porous medium were obtained from his analysis as limiting cases. A few studies concerning finite-amplitude convection in a two-component fluid-saturated porous layer are also available in the literature. The nonlinear stability of thermohaline convection in a horizontal porous layer heated from below has been considered by Rudraiah, Shrimani & Friedrich (1982). The critical Rayleigh number, for the onset of finite-amplitude convection, was derived using a truncated representation of the Fourier series. The effects of Prandtl, Lewis and Darcy numbers on convection are discussed by these authors. Thermohaline convective flows through a square porous cavity heated from below have been investigated numerically by Rosenberg & Spera (1992) for various boundary and initial conditions. Parametric relationships, obtained by these authors for *Nu* and *Sh* for a cavity salted from below, were found to be in good agreement with the results of Trevisan & Bejan (1987). Chen & Chen (1993) considered nonlinear two-dimensional double-diffusive fingering convection in a saturated porous medium. The stability boundaries which separate regions of different types of convective motion were identified in terms of solute and thermal Rayleigh numbers.

The onset and development of convection in a horizontal porous enclosure have been investigated by Mamou & Vasseur (1999) using the linear and nonlinear perturbation theories. Both the imposition of Dirichlet or Neumann boundary conditions on temperature and solute are considered by these authors. Analytical solutions are derived to predict the flow behaviour. The existence of multiple solutions, for a given set of governing parameters, is demonstrated for the case of opposing flows. The onset of double-diffusive convection in a porous layer, with mixed boundary conditions for heat and solute applied on the horizontal boundaries, has been investigated by Mahidjiba, Mamou & Vasseur (2000) on the basis of the linear stability theory. Numerical results for the finite-amplitude convection, obtained by solving numerically the full governing equations, demonstrate that subcritical convection is possible. The case of a horizontal porous layer heated horizontally and salted from the bottom was considered by Kalla *et al.* (2001). It was demonstrated analytically and numerically that multiple stable solutions are possible for this situation.

A few studies have also concerned the Soret effect in a horizontal porous layer filled with a binary fluid. The linear stability theory was used by Patil & Rudraiah (1980) and Brand & Steinberg (1983*a*) to investigate the instabilities in a layer heated from below or from above. The possibility of an oscillatory convective instability when heating from above was pointed out. Nonlinear effects in the convective instability near the threshold were discussed by Brand & Steinberg (1983*b*). The convective instability of a fluid mixture in a porous medium with a time-dependent temperature gradient was investigated by Ouarzazi & Bois (1994) using a linear asymptotic analysis. The onset of Soret-driven convection in a porous layer was studied by Sovran, Charrier-Mojtabi & Mojtabi (2001). When the layer is heated from below, it was found that convection occurs via a stationary bifurcation or via a Hopf bifurcation, depending on the value of the governing parameters. The Soret effect on natural convection in a horizontal porous layer subjected to uniform fluxes of heat was considered by

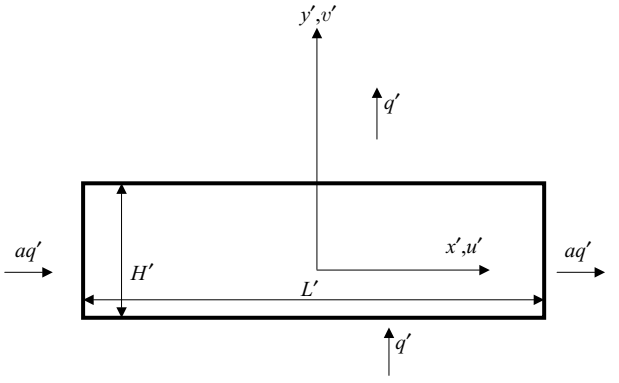


FIGURE 1. Schematic diagram of the physical model and coordinate system.

Bourich *et al.* (2002). The existence of subcritical convection was demonstrated by these authors. A comparison between double-diffusive and Soret-induced convection in a shallow horizontal porous layer was made by Bahloul, Boutana & Vasseur (2003). The thresholds for finite-amplitude oscillatory and monotonic convection instabilities were determined in terms of the governing parameters. An analytical solution, valid in the limit of a shallow layer, was proposed and found to be in good agreement with numerical simulations. A linear stability of the flow predicted by the analytical model, was conducted in order to predict the thresholds for Hopf bifurcation.

The aim of the present analysis is to study the Soret-induced convection in a horizontal porous enclosure subjected to cross heat fluxes. An analytical solution is proposed for a shallow cavity on the basis of the parallel-flow approximation. The results are verified numerically by solving the full nonlinear set of governing equations with a control volume method.

The paper is organized as follows: in the next section, the physical system is described and a mathematical model of the problem is derived. The control volume approach used to solve the full governing equations is discussed in § 3. The analytical model, based on the parallel-flow approximation, is proposed § 4. Section 5 deals with the particular situation of the buoyancy forces induced when the thermal and solutal effects are opposing each other and of equal intensity. For this situation, a linear stability of the rest state is carried out to predict the critical Rayleigh number defining the onset of motion from the rest state. Finally, concluding remarks are given in § 6.

## 2. Mathematical model

The system to be studied consists of a horizontal rectangular porous cavity with an aspect ratio $A = L'/H'$, where $L'$ is the length and $H'$ the height of the cavity, filled with an incompressible Newtonian binary fluid mixture (figure 1). The bottom and top horizontal impermeable boundaries are subject to vertical uniform fluxes of heat $q'$. Also, a uniform heat flux $aq'$, where $a$ is a constant, is applied on the two vertical impermeable walls.

Assuming that the temperature and concentration gradients are small, as required by the Boussinesq approximation, the diffusive heat and mass fluxes $q'$ and $j'$ are given by De Groot & Mazur (1962):

$$q' = -k\nabla T', \tag{2.1}$$

$$j' = -\rho D\nabla N - \rho D' N(1-N)\nabla T', \tag{2.2}$$

where $k$ is the thermal conductivity, $D$ is the mass diffusivity and $D'$ the phenomenological coefficient for the Soret effect. All those coefficients are assumed to be constant in the considered range of temperature $T'$ and mass fraction $N$.

The density $\rho$ of the binary solution is assumed to be a linear function of temperature and composition, i.e.

$$\rho = \rho_0[1 - \beta'_T(T' - T'_0) - \beta_N(N - N_0)], \tag{2.3}$$

where $\rho_0$ is the fluid mixture density at temperature $T' = T'_0$ and mass fraction $N = N_0$ and $\beta'_T$ is the thermal expansion coefficient and $\beta_N$ the solute analogue of $\beta'_T$. The subscript 0 refers to the condition at the origin of the coordinate system. The mass fraction of the denser component of the mixture, $N_0$, is assumed to be initially uniform.

The equations expressing conservation of momentum, energy and species are given by:

$$\nabla^2\Psi' = -\frac{gK\beta'_T}{\nu}\frac{\partial}{\partial x'}\left(T' + \frac{\beta_N}{\beta'_T}N\right), \tag{2.4}$$

$$\left(\rho C_p\right)\frac{\partial T'}{\partial t'} + \left(\rho C_f\right)\boldsymbol{V}'\cdot\nabla T' = k\nabla^2 T', \tag{2.5}$$

$$\phi\frac{\partial N}{\partial t'} + \boldsymbol{V}'\cdot\nabla N = D\nabla^2 N + D'N_0(1 - N_0)\nabla^2 T', \tag{2.6}$$

where $\boldsymbol{V}'$ is the Darcy velocity, $g$ the acceleration due to gravity, $\nu$ the kinematic viscosity, $K$ and $\phi$ are, respectively, the permeability and the porosity of the porous medium, $\left(\rho C_p\right)$ and $\left(\rho C_f\right)$ are, respectively, the heat capacity of the saturated porous medium and the fluid and $\Psi'$ is the streamfunction. As usual, we have $u' = \partial\Psi'/\partial y'$ and $v' = -\partial\Psi'/\partial x'$, such that the conservation of mass is satisfied.

In deriving equation (2.6) it has been assumed that the cross-diffusion Soret coefficient $N(1-N)$ is constant, not subject to fluctuation, and equal to its initial value $N_0(1-N_0)$. It has been argued in the past that this assumption is more or less realistic for equimolar mixtures (Platten & Legros 1984) or when the Soret effect is relatively weak (Bergeon *et al.* 1998). In any case, the simplified mass balance equation (2.6) is currently invoked in most of the recent available studies on this topic. This is the case not only for Soret-induced convection in porous media, but also for Soret-induced convection in liquids (see for instance Batiste, Alonso & Mercader 2004; Bourich *et al.* 2004, 2005; and Piquer *et al.* 2005).

The following dimensionless variables (primed quantities are dimensional) are used:

$$\left.\begin{array}{lll} (x, y) = (x', y')/H', & (u, v) = (u', v')H'/\alpha, & t = t'\alpha/H'^2\sigma, \\ T = (T' - T'_0)/\Delta T', & \Delta T' = q'H'/k, & C = N/\Delta N, \\ \Delta N = \Delta T' N_0(1 - N_0)D'/D, & \varepsilon = \phi/\sigma, & \Psi = \Psi'/\alpha, \end{array}\right\} \tag{2.7}$$

where $t'$ is the time, $\alpha = k/(\rho C_f)$ the thermal diffusivity. Also, $\sigma = (\rho C_p)/\left(\rho C_f\right)$ is the heat capacity ratio.

The governing equations that describe the system behaviour are expressed in terms of streamfunction, temperature and concentration, in dimensionless form, as follows:

$$\nabla^2\Psi = -R_T\left(\frac{\partial T}{\partial x} + \varphi\frac{\partial C}{\partial x}\right), \tag{2.8}$$

$$\frac{\partial T}{\partial t} + u\frac{\partial T}{\partial x} + v\frac{\partial T}{\partial y} = \nabla^2 T, \tag{2.9}$$

$$\varepsilon\frac{\partial C}{\partial t} + u\frac{\partial C}{\partial x} + v\frac{\partial C}{\partial y} = \frac{1}{Le}(\nabla^2 C - \nabla^2 T). \tag{2.10}$$

The boundary conditions are slip conditions and a constant heat flux applied on the boundaries. Also, the normal mass flux, (2.2), is zero on the walls. Thus, we obtain the following system for the boundary conditions:

$$\left.\begin{aligned} x = \pm\tfrac{1}{2}A, \quad \Psi = 0, \quad \frac{\partial T}{\partial x} = \frac{\partial C}{\partial x} = -a, \\ y = \pm\tfrac{1}{2}, \quad \Psi = 0, \quad \frac{\partial T}{\partial y} = \frac{\partial C}{\partial y} = -1. \end{aligned}\right\} \tag{2.11}$$

Equations (2.8)–(2.11) indicate that the present problem is governed by six dimensionless parameters, namely the thermal Rayleigh number $R_T$, the separation parameter $\varphi$, the Lewis number $Le$, the normalized porosity $\varepsilon$, the cavity aspect ratio $A$ and the constant $a$, defined as

$$\left.\begin{aligned} R_T = \frac{g\beta_T' K \Delta T' H'}{\alpha \nu}, \quad \varphi = \frac{\beta_N \Delta N}{\beta_T' \Delta T'}, \\ Le = \frac{\alpha}{D}, \quad A = \frac{L'}{H'}, \quad \varepsilon = \frac{\phi}{\sigma}. \end{aligned}\right\} \tag{2.12}$$

It is observed that for $\varphi > 0$, both the thermal and solutal buoyancy forces are cooperative whereas for $\varphi < 0$ they are opposing each other.

The vertical temperature and mass fraction across the enclosure are expressed in terms of the Nusselt and Sherwood numbers, respectively, defined as

$$Nu = \frac{1}{\Delta T}, \quad Sh = \frac{1}{\Delta C}, \tag{2.13}$$

where $\Delta T = T(0, -1/2) - T(0, 1/2)$ and $\Delta C = C(0, -1/2) - C(0, 1/2)$ are the temperature and concentration differences, evaluated at $x = 0$.

In the above equations, $Nu$ has its usual meaning, whereas $Sh$ is related to the concentration distribution within the cavity induced by the Soret effect and by convection.

## 3. Numerical solution

Solution of the flow field and concentration distributions within the enclosure may be found using a control volume approach and adapted mesh grid. The governing equations for the streamfunction, (2.8), and temperature and concentration, (2.9) and (2.10), are first discretized using the classical power law scheme. The discretized equations for $\Psi$, $T$ and $C$ are then solved at each time step using the last available field values, until convergence to a steady or an oscillating state is achieved. The energy and concentration equations (2.9) and (2.10) were solved using an alternating direction implicit method (ADI). The streamfunction field was obtained from (2.8) using the successive over-relaxation method (SOR) and known temperature and concentration distributions. The mesh size required for sufficient numerical accuracy depends mainly on the thermal and solutal Rayleigh numbers and the aspect ratio of the porous layer. The nodal points were skewed in the $x$ and $y$ directions to obtain a greater concentration of points near the solid boundaries. Numerical tests, using various mesh sizes, were done for the same conditions in order to determine the best compromise between the accuracy of the results and use of computer time. Besides the usual control, the accuracy of computations was estimated using the energy and mass fraction conservation within the system. Typical numerical results are presented in figure 2 for $R_T = 30$, $\varphi = -0.1$, $Le = 10$, $a = 0.05$ and $A = 8$. On the graph streamlines,

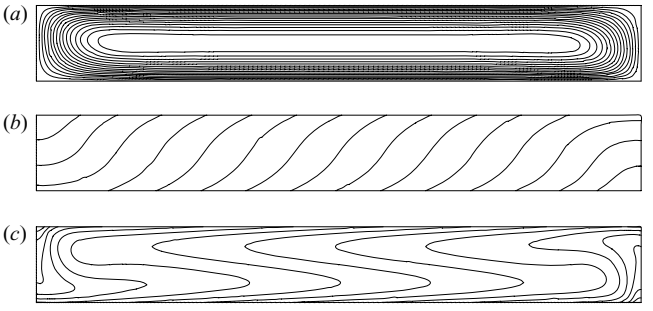


FIGURE 2. Contour lines of ($a$) streamfunction, ($b$) temperature and ($c$) mass fraction for $R_T = 30$, $\varphi = -0.1$, $Le = 10$, $a = 0.05$ and $A = 8$: $\Psi_0 = 1.60$, $Nu = 1.89$, $Sh = 6.47$.

isotherms and isoconcentrates are presented from top to bottom. The results show that for a long shallow cavity ($A \gg 1$) the flow in the core region of the enclosure is essentially parallel with a linearly dependency of the temperature and mass fraction in the horizontal direction. The analytical solution, developed in the following section, will rely on these observations.

## 4. Analytical solution for the convective flow

An approximate solution can be sought for a long shallow cavity ($A \gg 1$). In this limit, as discussed in detail by Bahloul *et al.* (2003) and other authors, the flow in the central portion of the cavity can be assumed to be parallel and in the $x$-direction. Thus we have

$$\Psi(x, y) = \Psi(y) \tag{4.1}$$

in the core region of the enclosure.

As the fluid moves with a constant velocity in the core part of the cavity, the uniform heat flux $q'$ at the walls increases its temperature linearly. There is, however, an unknown transverse variation of the temperature in the $y$-direction. Thus, we have

$$T(x, y) = C_T x + \theta_T(y), \tag{4.2}$$

where $C_T$ is the temperature gradient along the $x$-direction.

In a similar way, the mass fraction distribution in the core of the cavity can be expressed as

$$C(x, y) = C_C x + \theta_C(y), \tag{4.3}$$

where $C_C$ is the mass fraction gradient along the $x$-direction.

Substituting the above equations into the steady form of equations (2.8)–(2.10), we obtain

$$\frac{\mathrm{d}^2\Psi}{\mathrm{d}y^2} = -R_T\,(C_T + \varphi C_C)\,, \tag{4.4}$$

$$\frac{\mathrm{d}^2\theta_T}{\mathrm{d}y^2} = C_T \frac{\mathrm{d}\Psi}{\mathrm{d}y}, \tag{4.5}$$

$$\frac{\mathrm{d}^2\theta_C}{\mathrm{d}y^2} = (LeC_C + C_T)\frac{\mathrm{d}\Psi}{\mathrm{d}y}. \tag{4.6}$$

The parallel-flow approximation is only applicable in the core of the enclosure. Flow in the end regions is much more complicated. For this reason, the thermal

boundary conditions in the $x$-direction, (2.11), cannot be applied directly with this approximation. Following Bejan & Tien (1978) and Kimura, Vynnycky & Alavyoon (1995), we can, however, impose an equivalent energy flux condition in that direction, such that one obtains

$$C_T + a = \int_{-1/2}^{1/2} \frac{\mathrm{d}\Psi}{\mathrm{d}y}\theta_T \,\mathrm{d}y. \tag{4.7}$$

Similarly, for the mass fraction it is found that

$$C_C - C_T = \int_{-1/2}^{1/2} \frac{\mathrm{d}\Psi}{\mathrm{d}y}\theta_C \,\mathrm{d}y. \tag{4.8}$$

The solution of (4.4)–(4.6), satisfying boundary conditions (2.11) is

$$\Psi = \Psi_0(1 - 4y^2), \tag{4.9}$$

$$\theta_T = \frac{C_T\Psi_0}{3}(3y - 4y^3) - y, \tag{4.10}$$

$$\theta_C = \frac{(LeC_C + C_T)\Psi_0}{3}(3y - 4y^3) - y, \tag{4.11}$$

where

$$\Psi_0 = \tfrac{3}{2}\bar{R}_T(C_T + \varphi C_C), \quad \bar{R}_T = R_T/R^{sup}, \quad R^{sup} = 12, \tag{4.12}$$

and where the reason for the introduction of the constant $R^{sup}$ will be explained in the following section.

Substituting (4.9)–(4.11) into (4.7) and (4.8) and integrating, yields

$$C_T = \frac{4b\Psi_0 - 3ab}{3\left(\Psi_0^2 + 2b\right)}, \tag{4.13}$$

$$C_C = \frac{4bLe\Psi_0 + 3C_T\left[Le\Psi_0^2 - b(1 - 1/Le)\right]}{3(Le^2\Psi_0^2 + 2b)}, \tag{4.14}$$

where $b = 15/16$.

Substituting the above values of $C_T$ and $C_C$ into the expression for $\Psi_0$, (4.12), the following fifth-order polynomial is obtained

$$f(\Psi_0, R_T) = \Psi_0\left[Le^4\Psi_0^4 - 2bLe^2d_1\Psi_0^2 - b^2d_2\right] + d_3\Psi_0^2 + d_4 = 0, \tag{4.15}$$

where

$$\left.\begin{aligned} d_1 &= \bar{R}_T Le^2 - (Le^2 + 1), \quad d_2 = 4\bar{R}_T Le^2[1 + \varphi(Le + 1)] - 4Le^2, \\ d_3 &= 3\bar{R}_T abLe^3[Le - \varphi], \quad d_4 = 6\bar{R}_T ab^2Le^2[1 + \varphi] \end{aligned}\right\} \tag{4.16}$$

For a given set of the governing parameters, $R_T$, $a$, $Le$ and $\varphi$, the above expression can be solved numerically, using for instance a Newton–Raphson scheme, to obtain $\Psi_0$. Then the values of $C_T$ and $C_C$ can be evaluated from (4.13) and (4.14), respectively.

Substituting (4.10) and (4.11) into (2.13), it is found that the Nusselt and Sherwood numbers are given, respectively, by

$$Nu = 6\frac{\Psi_0^2 + 2b}{\Psi_0^2 + 4b(a\Psi_0 + 3)}, \tag{4.17}$$

$$Sh = 6\frac{Le^2\Psi_0^2 + 2b}{Le^2\Psi_0^2 + 4b(aLe\Psi_0 + 3) - 6b(1 + Le)Nu/(Nu - 1)}. \tag{4.18}$$

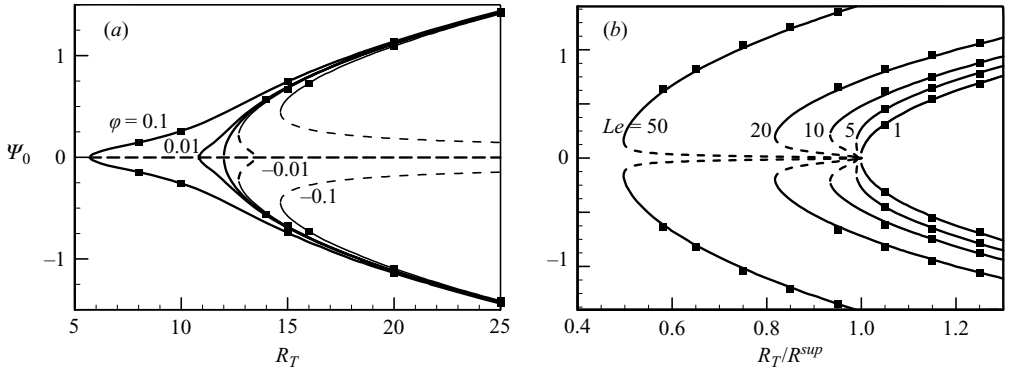


FIGURE 3. Bifurcation diagrams as predicted by the parallel-flow approximation for $a = 0$: ($a$) effect of $\varphi$ for $Le = 10$, ($b$) effect of $Le$ for $\varphi = -0.01$. —, - - -, analytical; ■, numerical.

## 5. Results and discussion

### 5.1. *Effect of parameter $\varphi$ on convection*

In this section, the effect of the separation parameter $\varphi$ on finite-amplitude convection, as predicted by the parallel-flow approximation, is compared with the numerical results obtained by solving the full governing equations. Convection in the absence of side heating, for which the solution takes the form of a standard Bénard bifurcation, is first considered. Then, the imperfection brought by the side heating to the bifurcation is investigated.

#### 5.1.1. *Convection in the absence of side heating ($a = 0$)*

In the absence of side heating, convection in the fluid layer is driven solely by the vertical gradients of heat and solute. For this situation, the velocity, temperature and mass fraction fields and Nusselt and Sherwood numbers are predicted by (4.9)–(4.12) and (4.17) and (4.18) in which the values of $C_T$ and $C_C$ are obtained by setting $a = 0$ in (4.13) and (4.14). From (4.15), it is readily found that the flow intensity $\Psi_0$ is given by

$$\Psi_0 = \pm \frac{\sqrt{b}}{Le}\left[d_1 \pm \sqrt{d_1^2 + d_2}\right]^{1/2}, \tag{5.1}$$

where

$$\begin{aligned} d_1 &= \bar{R}_T Le^2 - (Le^2 + 1), \\ d_2 &= 4\bar{R}_T Le^2[1 + \varphi(Le + 1)] - 4Le^2. \end{aligned} \tag{5.2}$$

The signs + and − outside the brackets refer to the possible occurrence of counter-clockwise and clockwise circulations, respectively. Inside the brackets, they refer to stable and unstable branches, respectively.

The conditions $d_1 < 0$ and $d_2 = 0$ yield the critical Rayleigh number for the onset of supercritical convection $R_{TC}^{sup}$, characterized by a transition from the quiescent state to a convective regime occurring through zero flow amplitude ($\Psi_0 = 0$), as

$$R_{TC}^{sup} = \frac{R^{sup}}{[1 + \varphi(Le + 1)]}. \tag{5.3}$$

Figure 3($a$) shows typical bifurcation diagrams for $\Psi_0$ as a function of $R_T$ and $\varphi$ for $Le = 10$. The analytical solution, predicted by the present theory, is represented by the solid (stable) and dashed (unstable) lines and is seen to be in good agreement with the numerical results depicted by solid squares. The case of pure thermal convection

($\varphi = 0$) will be discussed first. For this situation, figure 3($a$) indicates that a pitchfork bifurcation occurs at a supercritical Rayleigh number $R_{TC}^{sup} = 12$, as predicted by (5.3) and in agreement with Nield (1967). The way in which this pitchfork bifurcation is affected by the Soret effect is illustrated for various values of $\varphi$. The case $\varphi > 0$, namely $\varphi = 0.01$, for which both the thermal and solutal buoyancy forces are destabilizing is considered first. For $R_T$ between the thermal-solutal threshold ($R_{TC}^{sup} = 10.81$) and the thermal one ($R_{TC}^{sup} = 12$), it is seen that the magnitude of the resulting flow field (i.e. of $\Psi_0$) is relatively weak. However, as the value of $R_T$ is made larger than the pure thermal threshold, the flow becomes much stronger. The contour lines of streamfunction, temperature and mass fraction (not presented here) indicate that for this situation the convective flow is driven by the temperature gradients, the mass fraction in the central part of the cavity being almost uniform. This is due to the large mixing resulting from the strong convective motion induced by the thermal-dominated regime. On the other hand, for $\varphi < 0$, the destabilizing thermal buoyancy forces are opposed to the stabilizing solutal influence. The resulting curve (for $\varphi = -0.01$) indicates the occurrence of a subcritical bifurcation for which the onset of convection occurs through finite-amplitude convection. The subcritical Rayleigh number $R_{TC}^{sub}$ at which such flows are induced can be obtained, from (5.1) and (5.2) from the conditions $d_1 > 0$ and $d_1^2 + d_2 = 0$, as

$$R_{TC}^{sub} = \frac{(1 + Le)R^{sup}}{Le^2}[Le - 2\varphi - 1 + 2\sqrt{\varphi(\varphi - Le + 1)}]. \tag{5.4}$$

It is observed that, although the thermal and solutal regimes are also present for this situation, the solutal branches depicted as dashed lines are now unstable. They are connected with stable thermal branches by saddle-node bifurcations. Also, they are connected to the supercritical Rayleigh number $R_{TC}^{sup}$ provided that this latter is greater than zero. For instance, for $\varphi = -0.01$, the solutal branches indicate that $\Psi_0 = 0$ at a supercritical Rayleigh number $R_{TC}^{sup} = 13.48$. This situation yields five solutions (two stable and two unstable convective flows, and a purely diffusive flow ($\Psi_0 = 0$) which is stable up to the supercritical Rayleigh number $R_{TC}^{sup}$. However, according to (5.3), when $\varphi > -0.091$ the supercritical Rayleigh number is negative and the solutal branches tend towards zero only as the value of $R_T$ tends asymptotically towards infinity. For this situation, convection can occur for $R_T < 0$ (cavity heated from the top) provided that $|R_T| > |R_{TC}^{sup}|$.

The influence of the Lewis number on the bifurcation character is illustrated in figure 3($b$) for $\varphi = -0.01$. According to the present solution it can be shown that the condition

$$\varphi < \varphi_c = \frac{1}{(Le + 1)(Le^2 + 1)} \tag{5.5}$$

must be satisfied for the existence of subcritical convection. Thus for the present case, the Lewis number expressing the transition from a supercritical to a subcritical bifurcation is $Le = 4.25$. As can be observed from the graph, the bifurcation is supercritical when $Le < 4.25$ (as illustrated by the curve for $Le = 1$) and subcritical when $Le > 4.25$.

5.1.2. *Convection in the presence of side heating ($a \neq 0$)*

The imperfection brought by the side heating to the bifurcation curves discussed above is now investigated. Because of the buoyant torque $\nabla\rho \times \boldsymbol{g}$, the hydrostatic state cannot be realized (at least exactly) with the horizontally imposed temperature gradient. Thus, the conductive state in the absence of side heating degenerates into

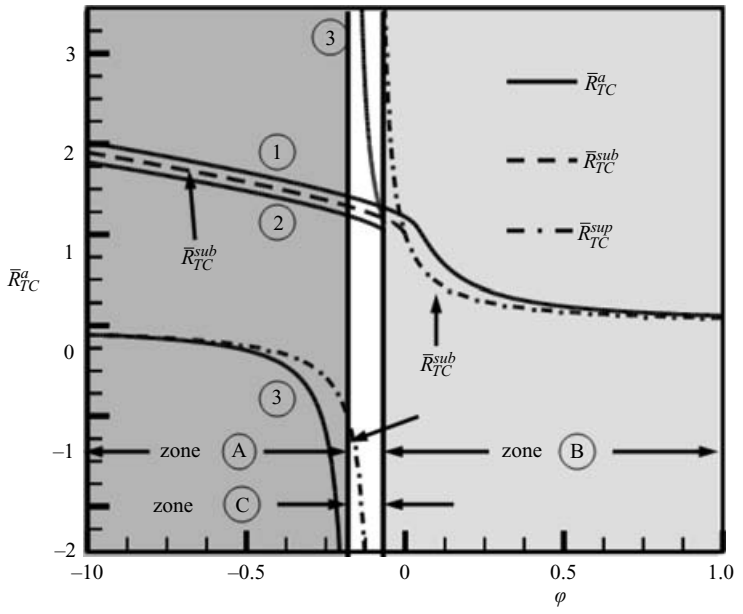


FIGURE 4. Critical Rayleigh number $\overline{R}^a_{TC}$ as a function of $\varphi$ for the case $Le = 10$ and $a = 0.05$.

a 'pseudoconductive' state. The influence of side heating on the convective state is discussed below.

Side heating is expected to affect the critical Rayleigh numbers for the onset of convection. These critical Rayleigh numbers, which depend upon the parameters $a$, $Le$ and $\varphi$, can be deduced easily from the present theory. For subcritical Rayleigh number, the derivative of $R_T$ with respect to $\Psi_0$ should be cancelled in (4.15). It can be demonstrated easily that $\partial R_T/\partial\Psi_0$ corresponds to $\partial f/\partial\Psi_0 = 0$, such that one obtains

$$g(\Psi_0) = 5Le^4\Psi_0^4 - 6bd_1Le^2\Psi_0^2 - b^2d_2 + 2d_3\Psi_0 = 0. \tag{5.6}$$

For a given set of the governing parameters, i.e. $a$, $Le$ and $\varphi$, the system of equations (5.1) and (5.6) can be solved numerically to obtain $R^a_{TC}$ and $\Psi^a_0$.

Figure 4 shows the subcritical Rayleigh number $\overline{R}^a_{TC}$ $(= R^a_{TC}/R^{sup})$ as a function of $\varphi$ for $a = 0.05$ and $Le = 10$, as predicted by (5.6). The results indicate the existence of three different curves identified by the symbols 1, 2 and 3. For completeness, the critical Rayleigh numbers for the onset of motion in the absence of side heating ($a = 0$), namely $\overline{R}^{sup}_{TC}$ $(= R^{sup}_{TC}/R^{sup})$, (5.3), and $\overline{R}^{sub}_{TC}$ $(= R^{sub}_{TC}/R^{sup})$, (5.4), are also included in that graph. In the presence of side heating, the subcritical Rayleigh number $\overline{R}^{sub}_{TC}$ degenerates into two distinct subcritical Rayleigh numbers, namely $\overline{R}^{a,1}_{TC} > \overline{R}^{sub}_{TC}$ and $\overline{R}^{a,2}_{TC} < \overline{R}^{sub}_{TC}$. As discussed above, in the presence of side heating, a convective state is always possible (except for the case $\varphi = -1$ for which convection occurs only above a subcritical Rayleigh number). On the other hand, the supercritical Rayleigh number $\overline{R}^{sup}_{TC}$ degenerates into the subcritical Rayleigh number $\overline{R}^{a,3}_{TC}$. It will be shown that $\overline{R}^{a,3}_{TC} > 0$ is the critical Rayleigh number for the existence of the 'pseudoconductive' state, whereas $\overline{R}^{a,3}_{TC} < 0$ is the critical Rayleigh number corresponding to the threshold below which multiple solutions may exist in the case of a cavity heated from the top

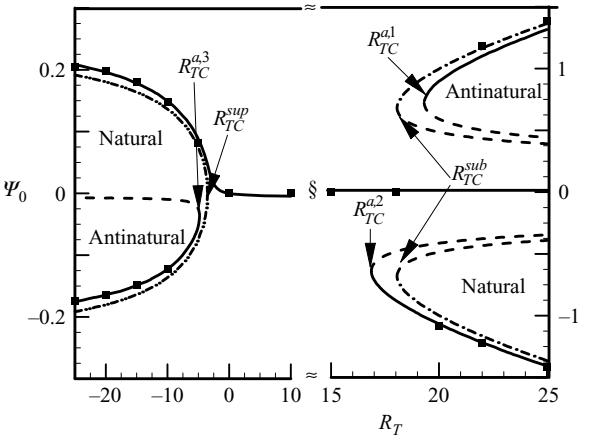


FIGURE 5. Bifurcation diagram as a function of $R_T$ for $\varphi = -0.4$, $Le = 10$ and $a = 0.05$: flow intensity $\Psi_0$. —, - - -, analytical; ■, numerical.

($R_T < 0$). It will be demonstrated also that for $\overline{R}_{TC}^{a,3} < 0$, the 'pseudoconductive' state, in the case of a cavity heated from the bottom, always exists. Figure 4 shows three different domains: a domain with two positive subcritical Rayleigh numbers and one negative subcritical Rayleigh number (zone A); a domain with one subcritical Rayleigh number (zone B); and a domain with three positive subcritical Rayleigh numbers (zone C). These three cases will be discussed in the following graphs.

Figure 5 illustrates the bifurcation curves obtained for $\varphi = -0.4$, $Le = 10$ and $a = 0.05$ (zone A). The dotted lines correspond to a pure Bénard situation ($a = 0$). As can be seen from figures 4 and 5, in the absence of side heating, the critical Rayleigh number for the onset of supercritical convection occurs for a negative value of the Rayleigh number (cavity heated by the top), namely $R_{TC}^{sup} = -3.53$, and the transition to convection occurs through a subcritical bifurcation at $R_{TC}^{sub} = 18.06$ when the cavity is heated from the bottom. Thus, figure 5 exemplifies how the side heating affects both supercritical ($R_T < 0$ in this case) and subcritical ($R_T > 0$ in this case) bifurcations. The imperfection brought by side heating is depicted by the solid and dashed lines. The results indicate that, when the value of $R_T$ is relatively small, both the analytical and the numerical results predict the existence of a clockwise circulation ($\Psi_0 < 0$). This type of flow, which numerically can develop from rest as the initial condition is the 'pseudoconductive' flow. For $R_T > 0$, it is observed that a first subcritical bifurcation appears at a critical Rayleigh number $R_{TC}^{a,2} = 16.73$, which is lower than that of the critical Rayleigh number for $a = 0$ (see figure 4). The results also reveal a second subcritical bifurcation at a second Rayleigh number $R_{TC}^{a,1} = 19.24$, larger than that of the critical Rayleigh number for $a = 0$, above which five solutions are theoretically possible for a given $R_T$. Thus, in addition to the expected 'natural' circulation, the upper curves indicate the possible existence of two anticlockwise circulations ($\Psi_0 > 0$). These flows, which circulate in a direction opposite to that imposed by the horizontal temperature gradient, are referred as 'antinatural' flows (see Sen, Vasseur & Robillard 1987). Figure 5 shows that the side heating, inducing a clockwise circulation, weakens the strength of the 'antinatural' flows, while it enhance that of the 'natural' flow. The lower branch of the 'natural' and 'antinatural' solutions, represented by a dashed line, is unstable and as such it has not been possible to obtain numerical confirmation of its existence. When the cavity is heated from the top ($R_T < 0$) the onset of

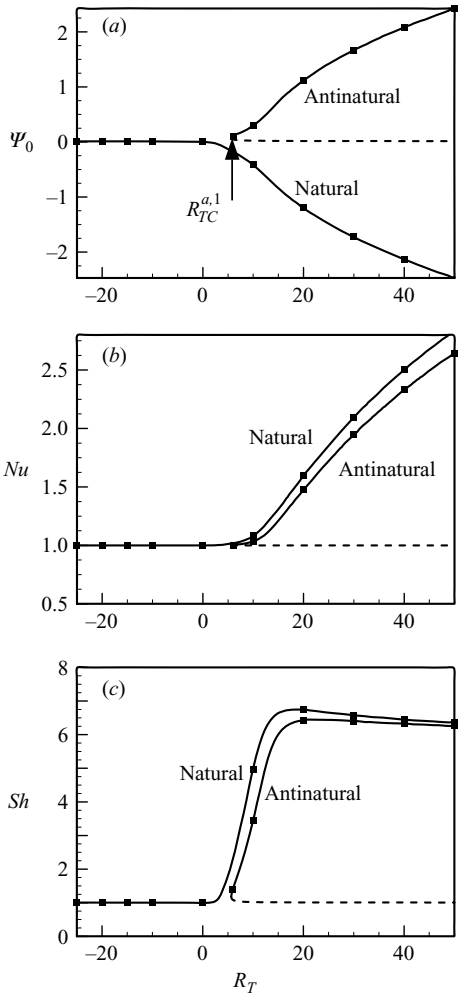


FIGURE 6. Bifurcation diagram as a function of $R_T$ for $\varphi = 0.2$, $Le = 10$ and $a = 0.05$: (*a*) flow intensity $\Psi_0$, (*b*) Nusselt number $Nu$ and (*c*) Sherwood number $Sh$. —, - - -, analytical; ■, numerical.

'antinatural' flow occurs now through a subcritical bifurcation at $R_{TC}^{a,3} = -6.30$ as compared with the supercritical Rayleigh number $R_{TC}^{sup} = -3.53$ characterizing the onset of supercritical convection when $a = 0$.

Figure 6 shows the effect of side heating on $\Psi_0$, the magnitude of the streamfunction at the centre of the cavity, and $Nu$ and $Sh$, the Nusselt and Sherwood numbers, as a function of $R_T$ for $\varphi = 0.2$, $Le = 10$ and $a = 0.05$ (zone B). For this situation, since the value of $\varphi$ is positive, both the thermal and solutal buoyancy forces are cooperating. Here again, when the value of $R_T$ is relatively small, both the analytical and the numerical results predict the existence of the 'pseudoconductive' flow and, for $R_T > R_{TC}^{a,1} = 5.67$, the results indicate that three solutions are theoretically possible for a given $R_T$, namely the 'natural' and the stable and unstable 'antinatural' branches. It was possible to verify numerically the analytically predicted 'antinatural' curve down to the vicinity of the turning point which occurs at $R_{TC}^{a,1}$. In figure 6, results are also presented for $R_T < 0$ for which stabilizing vertical temperature and mass fraction

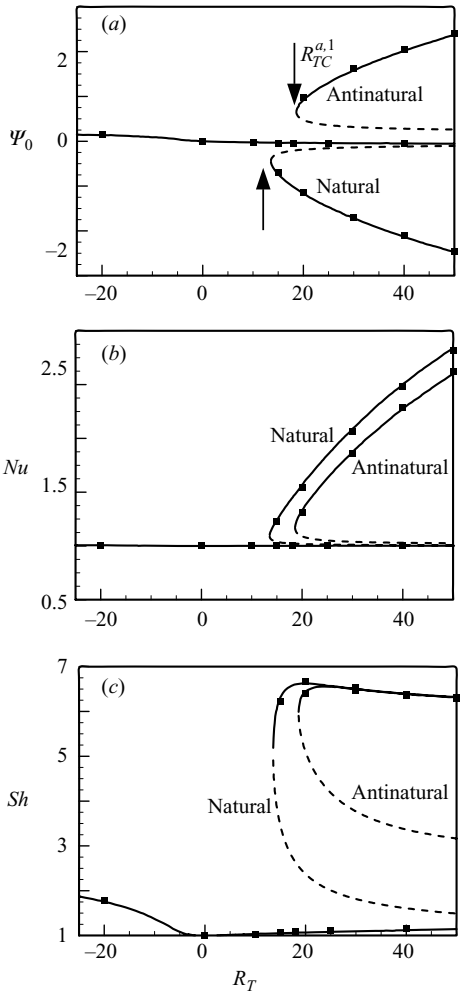


FIGURE 7. As figure 6, but for $\varphi = -0.2$.

gradients and negative destabilizing horizontal temperature and mass fraction gradients are now applied on the layer. This situation gives rise to a 'pseudoconductive' flow.

Figure 7 shows $\Psi_0$, $Nu$ and $Sh$ as a function of $R_T$ for $\varphi = -0.2$, $Le = 10$ and $a = 0.05$, i.e. when the thermal and solutal buoyancy forces are opposing each other (zone C). For $a = 0.05$ and negative values of $R_T$, for which the cavity is heated from the top and from the right-hand-side vertical wall, the only possible solution is an anticlockwise circulation ($\Psi_0 > 0$) corresponding to the 'pseudoconductive' flow. When the cavity is heated from the bottom and through the left-hand-side vertical wall ($R_T > 0$), the results indicate that for small values of $R_T$, the 'pseudoconductive' flow ($\Psi_0 < 0$) is the only solution. As the value of $R_T$ is made larger, the two convective branches discussed earlier, for $R_T > R_{TC}^{a,1} = 18.62$ and $R_{TC}^{a,2} = 13.57$ are progressively recovered. In the range $R_{TC}^{a,2} < R_T < R_{TC}^{a,1}$, three solutions, namely the 'pseudoconductive' and the stable and unstable 'natural' flows, coexist. When $R_T$ is made larger, it is seen from figure 7 that for $R_T > R_{TC}^{a,1}$, five solutions, three 'natural' and two 'antinatural' are possible, two of which are unstable.

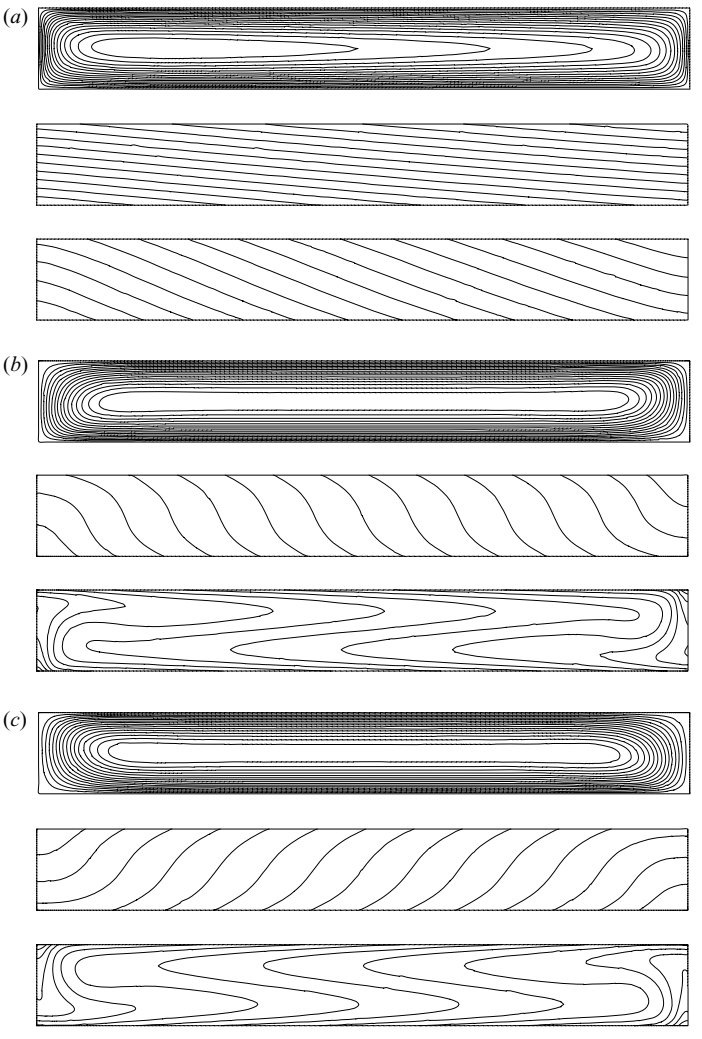


FIGURE 8. Contour lines of streamfunction (top), temperature (middle) and mass fraction (bottom) for $R_T = 25$, $\varphi = -0.2$, $Le = 10$, $a = 0.05$ and $A = 8$: (*a*) natural flow $\Psi_0 = -1.47$, $Nu = 1.85$, $Sh = 6.59$; (*b*) natural flow $\Psi_0 = -0.05$, $Nu = 1.00$, $Sh = 1.10$; (*c*) antinatural flow $\Psi_0 = 1.31$, $Nu = 1.63$, $Sh = 6.57$.

Numerical confirmation of the analytical model, and of the existence of multiple solutions is demonstrated in figure 7. This last point is also illustrated in figure 8 for the case $R_T = 25$, $\varphi = -0.2$, $Le = 10$ and $a = 0.05$. For this situation, three stable solutions were obtained, one of the solution being 'antinatural' and the two others 'natural'. Here again, an appropriate initial condition had to be used to simulate the three different solutions. Thus the weak diffusive type natural solution (figure 8*a*), was obtained using the rest state as the initial condition to initiate the numerical procedure. However, a convective flow pattern circulating in the appropriate direction was used as the initial condition to obtain the 'natural' and the 'antinatural' flows depicted in figure 8(*b*) and 8(*c*), respectively.

Another view of the effect of side heating intensity on the existence of multiple solutions is depicted in figure 9 for $Le = 10$ and various values of $R_T$. The case

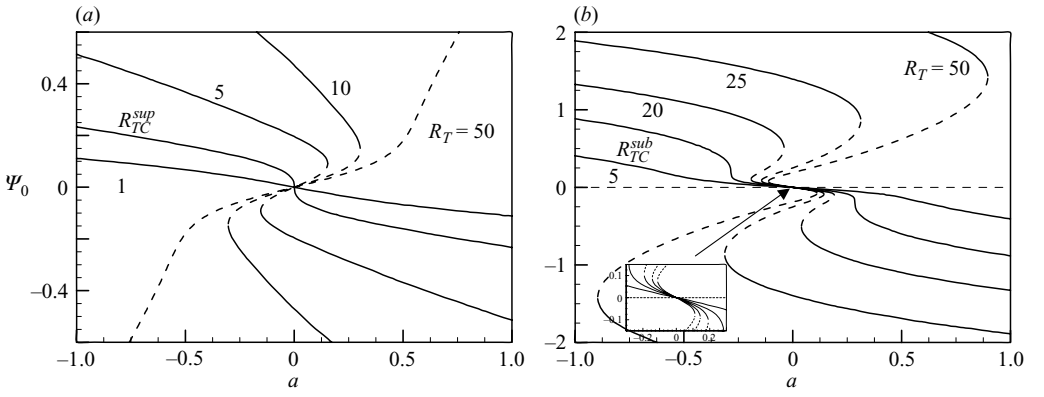


FIGURE 9. Flow intensity $\Psi_0$ as a function of $a$ for different values of $R_T$, $Le = 10$ and (a) $\varphi = 0.4$; (b) $\varphi = -0.2$.

$\varphi = -0.4$, for which the thermal and solutal buoyancy forces are cooperating is depicted in figure 9(*a*) and will be discussed first. In the absence of side heating ($a = 0$), convection is possible only above a supercritical Rayleigh number $R_{TC}^{sup} = 3.75$ as predicted by (5.3). Thus, for $R_T < R_{TC}^{sup}$, it can be seen from figure 9(*a*) that the resulting flow pattern corresponds to a 'natural' flow, circulating in the direction imposed by the side heating, i.e. clockwise (anticlockwise) for a positive (negative) value of $a$. Above the supercritical Rayleigh number, in the pure Bénard situation ($a = 0$), the resulting unicellular flow induced by the constant heat flux $q'$ rotates indifferently clockwise or counterclockwise. When a side heating $aq'$ is applied on the vertical walls of the cavity it can be seen from figure 8(*a*) that in addition to 'natural' flows, the existence of 'antinatural' flows is also possible provided that the constant $a$ is small enough for a given $R_T$. The second and fourth (first and third) quadrants represent the 'natural' ('antinatural') flows. Thus, for $R_T > R_{TC}^{sup}$ and for small values of the constant $a$, three values of $\Psi_0$ are possible. However, the inner 'antinatural' branch is unstable and is shown by broken lines.

Similar results obtained for $\varphi = -0.2$, i.e. when the thermal and solutal buoyancy forces are opposing each other, are presented in figure 9(*b*). For this situation, in the absence of side heating ($a = 0$), convection occurs through finite-amplitude motion when the Rayleigh number is above a subcritical Rayleigh number $R_{TC}^{sub} = 15.99$, as predicted by (5.4). Here again for $R_T < R_{TC}^{sub}$, figure 9(*b*) shows that the only possible flow is a 'natural' one circulating clockwise (anticlockwise) when $R_T$ is positive (negative). Above the subcritical Rayleigh number, in the pure Bénard situation ($a = 0$), four solutions (two stable and two unstable), corresponding to unicellular cells circulating indifferently clockwise or counterclockwise, are predicted by the analytical model. For $R_{TC}^{sub} < R_T < R_{TC}^{sup}$, and for small enough values of the constant $a$, a fifth solution corresponding to the 'pseudoconductive' flow is also possible.

All the numerical results reported so far indicate that the resulting flows are unicellular and parallel in the core of the cavity. This is the basis of the analytical model proposed in the present study. However, the numerical simulations have also revealed the existence of different flow structures and time periodic solutions that will now be discussed. Figure 10(*a*) displays the bifurcation diagram $\Psi_0$ versus $\varphi$ for $R_T = 25$, $Le = 10$ and $a = 0.05$. The upper branch and the lower one represent the

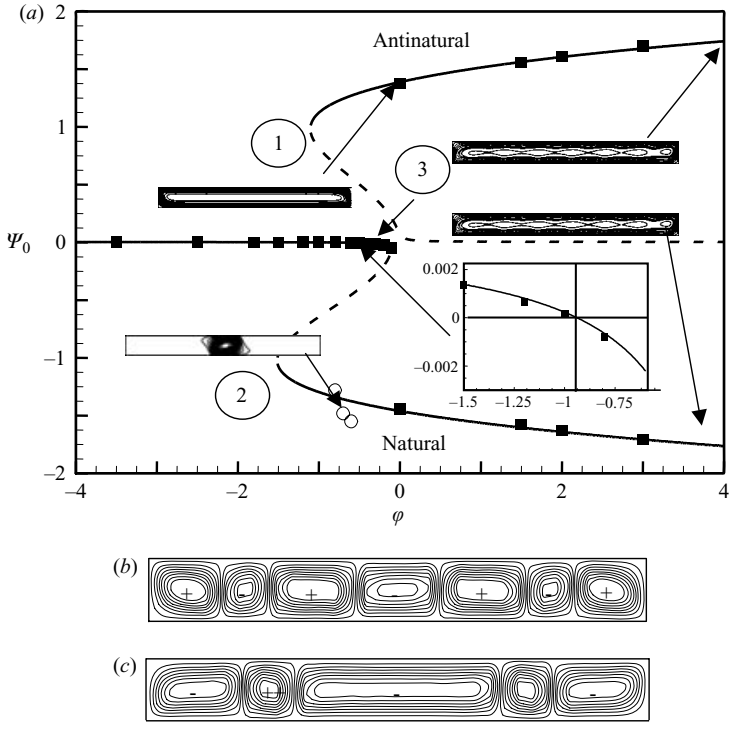


FIGURE 10. Bifurcation diagram as a function of $\varphi$ for $R_T = 25$, $Le = 10$ and $a = 0.05$: ($a$) flow intensity $\Psi_0$, and ($b$) and ($c$) contour lines of streamfunction for $R_T = -15$, $Le = 10$, $\varphi = -2.8$ and $a = 0.1$. Solutions ($b$) and ($c$) are obtained using different initial conditions. —, ---, analytical; ■, numerical.

'antinatural' and the 'natural' solutions, respectively, as predicted by the analytical model. Symbols 1, 2 and 3 refer to figure 4 and the range of existence of the 'antinatural', 'natural' and 'pseudoconductive' regimes. Numerical confirmation of the upper 'antinatural' branch is observed to be excellent in the range $-0.2 \leqslant \varphi \leqslant 3$. For $\varphi \leqslant -0.2$, a loss of stability of the 'antinatural' convection patterns occurs and the numerical solution evolves towards the most stable 'natural' lower branch. For $\varphi > 3$, it was found numerically that the flow becomes unsteady. The resulting flows pattern (figure 10$a$), is characterized by a slightly oscillating flow structure in the core of the cavity, surrounded by a steady unicellular parallel cell confined by the walls of the cavity. This type of flow was also observed numerically while studying the 'natural' branch ($\Psi_0 < 0$) for values of $\varphi \geqslant 4$. For $-1.52 < \varphi < -0.11$, it is seen that the present theory predicts the existence of three possible solutions for a given value of $\varphi$, one of these solutions (dashed lines) being unstable. The upper curve corresponds to the 'pseudoconductive' regime. For this situation, it was possible to obtain numerical results for values up to the upper turning point ($\varphi = -0.11$) connecting the 'pseudoconductive' and the unstable 'natural' branches. Although the strength of the convection $\Psi_0$, for the 'pseudoconductive' branch, is very small, the enlargement depicted in figure 10($a$) shows that the agreement between the numerical code used in that investigation and the analytical model is extremely good. Also, it can be seen that as the parameter encompass the value $-1$, the sign of $\Psi_0$ changes. This follows from the fact that $\Psi_0 = 0$ when $\varphi = -1$, for which the opposing thermal and solutal

buoyancy forces are equal. However, when $\varphi < -1$ ($\varphi > -1$), the thermal (solutal) buoyancy forces are predominant such that $\Psi_0 > 0$ ($< 0$). Numerical confirmation of the present analytical model, for the 'natural' branch, is obtained only for $0.1 < \varphi < 4$. It was not possible to obtain numerical results for values of $\varphi$ between 0.1 and $-1.52$ (for which a second turning point occurs). The numerical computations indicate that, as the value of $\varphi$ is decreased from $\varphi = 0.1$ (for which a parallel flow is obtained) to $\varphi = -1.5$, the resulting flow pattern changes drastically. Thus, as depicted in figure 10(*a*), the fluid is now stagnant almost everywhere in the cavity except at the centre where a very small cell exists. Finally, in the range $-0.11 < \varphi < 4$, the existence of both the 'pseudoconductive' and the 'natural' solutions is confirmed numerically.

Another type of steady non-parallel flow configurations was obtained in this study as illustrated in figures 10(*b*) and 10(*c*) for the case $R_T = -15$, $\varphi = -2.8$, $Le = 10$ and $a = 0.1$. Thus, starting the numerical procedure with a counterclockwise unicellular cell, yields the results shown in figure 10(*b*). The flow pattern consists in 7 cells of approximately equal size. The rotation of each cell is identified by a positive (counterclockwise) or a negative (clockwise) sign. Thus, it is observed that the flow is up the heated right-hand-side vertical wall and down the cooled left-hand-side vertical wall. On the other hand, figure 10(*c*) shows the results obtained upon using a clockwise unicellular cell as an initial condition. The flow patterns consist of only five cells, the size of the central cell being considerably larger than that of the other cells. Also, it is now observed that the flow is down and up the heated and the cooled vertical walls, respectively.

### 5.2. *Convection for the particular case ($\varphi = -1$)*

#### 5.2.1. *Onset of convection: the linear stability analysis*

In this section, the special case $\varphi = -1$, for which the buoyancy forces induced by the thermal and solutal effects are opposing each other and of equal intensity, is considered. It is noted that similar investigations have been reported in the past, for the case of a vertical cavity heated isothermally from the sides, by Traore & Mojtabi (1994) and Marcoux, Charrier-Mojtabi & Bergeron (1998). For this situation, the purely diffusive state $\Psi = 0$ and $T = C = -ax - y$ is a solution of the governing set of equations (2.8)–(2.10). The linear stability of this rest state, which is a direct consequence of the Soret effect, is now considered.

The solution of the perturbed equations of momentum, energy and solute diffusion is searched in normal modes, namely:

$$\left.\begin{aligned} \Psi(t, x, y) &= \Psi_0 \, \mathrm{e}^{pt} F(x, y), \\ \Theta(t, x, y) &= \Theta_0 \, \mathrm{e}^{pt} G(x, y), \\ \Phi(t, x, y) &= \Phi_0 \, \mathrm{e}^{pt} G(x, y), \end{aligned}\right\} \tag{5.7}$$

where $F(x, y)$ and $G(x, y)$ are space functions satisfying the boundary conditions describing the fields of $\Psi$, $\Theta$ and $\Phi$ at the onset of convection, $p$ is the growing rate of the perturbation and $\Psi_0$, $\Theta_0$ and $\Phi_0$ are unknown amplitudes.

This leads to the following set of equations:

$$\Psi_0 \nabla^2 F = -R_T(\Theta_0 - \Phi_0)\frac{\partial G}{\partial x}, \tag{5.8}$$

$$p\Theta_0 G - \Psi_0 \frac{\partial F}{\partial x} + a\Psi_0 \frac{\partial F}{\partial y} = \Theta_0 \nabla^2 G, \tag{5.9}$$

$$p\varepsilon\Phi_0 G - \Psi_0 \frac{\partial F}{\partial x} + a\Psi_0 \frac{\partial F}{\partial y} = \frac{1}{Le}(\Phi_0 - \Theta_0)\nabla^2 G. \tag{5.10}$$

The procedure to solve the above set of equations numerically has been discussed in detail by Mamou & Vasseur (1999). First, the Galerkin method is used to turn (5.8)–(5.10) into the weak formulation. Then, a finite-element method, based on the four-model cubic Hermite element, is used to obtain the following discretized set of linear equations:

$$\Psi_0[K]_{\Psi_0}\{F\} = R_T(\Theta_0 - \Phi_0)[B]\{G\}, \tag{5.11}$$

$$p\Theta_0[M]\{G\} + \Psi_0 L\{F\} = \Theta_0[K]\{G\}, \tag{5.12}$$

$$p\varepsilon\Phi_0[M]\{G\} + \Psi_0 L\{F\} = \frac{1}{Le}(\Phi_0 - \Theta_0)[K]\{G\}. \tag{5.13}$$

where $[B]$, $[K]$, $[K]_{\Psi_0}$, $[L]$ and $[M]$ are square matrices defined by:

$$\left.\begin{aligned} [B]^e &= \int_{\Omega^e} \frac{\partial \mathcal{N}_j}{\partial x}\mathcal{N}_i \,\mathrm{d}\Omega^e, & [K]^e &= [K]^e_{\Psi_0} = \int_{\Omega^e} \nabla\mathcal{N}_j \cdot \nabla\mathcal{N}_i \,\mathrm{d}\Omega^e, \\ [L]^e &= \int_{\Omega^e} \left(\frac{-\partial \mathcal{N}_j}{\partial x}\mathcal{N}_i + a\frac{\partial \mathcal{N}_j}{\partial y}\mathcal{N}_i\right)\mathrm{d}\Omega^e, & [M]^e &= \int_{\Omega^e} \mathcal{N}_j \cdot \mathcal{N}_i \,\mathrm{d}\Omega^e, \end{aligned}\right\} \tag{5.14}$$

$\Omega$ being the physical domain of integration.

From (5.11)–(5.13), the special case $p = 0$ yields the marginal state of instability for which the exchange of stability is valid. In this situation, using the fact that $\Phi_0 = (1 + Le)\Theta_0/Le$, the following eigenvalue problem is readily obtained:

$$[E - \lambda I]\{F\} = 0, \tag{5.15}$$

where $[E] = [K]^{-1}_{\Psi_0}[B][K]^{-1}[L]$ and $\lambda = -1/LeR_T$.

A non-trivial solution $\{F\} \neq 0$ is possible only if the determinant of $[E - \lambda I]$ is zero. In this way, (5.15) yields $m$ eigenvalues, $\lambda_i$, with their corresponding eigenvectors $\{F_i\}$, where $i = 1, m$. Rearranging the eigenvalues as $\lambda_1 < \lambda_2 \ll \lambda_m$, then the supercritical Rayleigh number for the onset of motion is given by:

$$R_{TC}^{sup} = -\frac{R_0}{Le}, \tag{5.16}$$

where $R_0 = 1/\lambda_m$ is a constant depending on the aspect ratio $A$ of the cavity and the constant $a$.

The effect of $a$ and $A$ on the numerically determined constants $R^0$ is illustrated in table 1. Most of the results presented in this table were obtained for a mesh size of $32 \times 12$ which is proved to be sufficient to model the problem accurately. For a given set of governing parameters, it was found that two different solutions are possible, one corresponding to $\lambda_1$ ($R^0 > 0$) and the other to $\lambda_m$ ($R^0 < 0$). In general, the two eigenvalues $\lambda_1$ and $\lambda_m$ are not equal, resulting in two different solutions. According to (5.16), the second solution ($R^0 < 0$) yields a positive value of the critical Rayleigh number $R_{TC}^{sup}$. This solution corresponds to the case of a layer heated from the bottom (figure 11). On the other hand, the first solution ($R^0 > 0$) yields a negative critical Rayleigh number $R_{TC}^{sup}$, for which the layer is heated from the top and cooled from the bottom. For this last situation, it is noticed that the lateral walls of the cavity are now heated and cooled from the left- and the right-hand sides, respectively. From table 1, it can be seen that, as expected, for a given strength of the side heating (i.e. $a$) the magnitude of the $R_{TC}^{sup}$ (i.e. $R^0$) decreases as the aspect ratio $A$ is made larger. On the other hand, it is found that, for a given value of $A$, $R^0$ decreases as the strength of the side heating is promoted. Naturally, when $a \to \infty$, it is seen that $\lambda_1 = -\lambda_m$ and the two resulting flow patterns are the mirror image of each other. The solution is not

| | | *A* | | | | |
|---|---|---|---|---|---|---|
| *a* | | 1 | 2 | 5 | 10 | $\infty$ |
| 0 | (1) | 22.94 | 14.79 | 12.45 | 12.11 | 12.00 |
| | (2) | $-\infty$ | $-\infty$ | $-\infty$ | $-\infty$ | $-\infty$ |
| 1 | (1) | 22.76 | 14.71 | 12.43 | 12.10 | 12.00 |
| | (2) | −1569.53 | −694.19 | −511.82 | −489.18 | −483.75 |
| 3 | (1) | 21.48 | 14.04 | 12.24 | 12.05 | 11.99 |
| | (2) | −145.01 | −87.98 | −73.69 | −71.73 | −71.23 |
| 5 | (1) | 19.42 | 12.86 | 11.77 | 11.60 | 11.56 |
| | (2) | −64.64 | −41.34 | −34.54 | −33.62 | −33.38 |
| 8 | (1) | 16.20 | 10.76 | 9.55 | 9.32 | 9.25 |
| | (2) | −34.26 | −22.10 | −18.45 | −17.94 | −17.81 |
| 10 | (1) | 14.35 | 9.49 | 8.25 | 8.05 | 7.99 |
| | (2) | −25.96 | −16.73 | −13.96 | −13.57 | −13.47 |
| 100 | (1) | 2.03 | 1.28 | 1.07 | 1.04 | 1.03 |
| | (2) | −2.14 | −1.35 | −1.12 | −1.09 | −1.08 |
| $\infty$ | (1) | $209/a$ | $131/a$ | $109/a$ | $106.5/a$ | $106/a$ |
| | (2) | $-209/a$ | $-131/a$ | $-109/a$ | $-106.5/a$ | $-106/a$ |

TABLE 1. Constant $R^0$ for various values of $a$ and $A$: (1) heated from the bottom; (2) heated from the top.

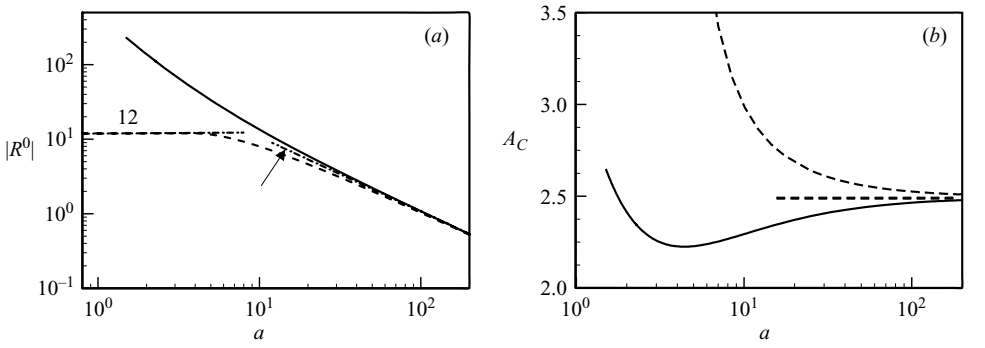


FIGURE 11. Case of an infinite layer ($A \to \infty$) for $\varphi = -1$: effect of side heating coefficient $a$ on ($a$) the constant $|R^0|$ and ($b$) the wavenumber $A_C$. —, heated from the top; - - -, heated from below.

affected by the relatively negligible vertical temperature and mass fraction gradients, but is driven essentially by the positive or the negative horizontal temperature and mass fraction gradients.

In the case of an infinite layer, the effect of $a$, on both the numerically determined constant $|R^0|$ and the critical wavenumber $A_C$, is depicted in figure 11. This particular case was simulated numerically by considering a cavity of aspect ratio $A_C$, subject to periodic boundary conditions applied on the right- and the left-hand vertical boundaries. In this way, $R^0$ was obtained for various values of $A_C$, the minimum corresponding to the critical Rayleigh number for the onset of convection in an infinite horizontal layer. For $a \to 0$, $R^0 \to 12$ when the cavity is heated from the bottom. Figure 11 indicates that for large values of $a$, i.e. when the horizontal temperature and mass fraction gradients are predominant over the vertical ones, the

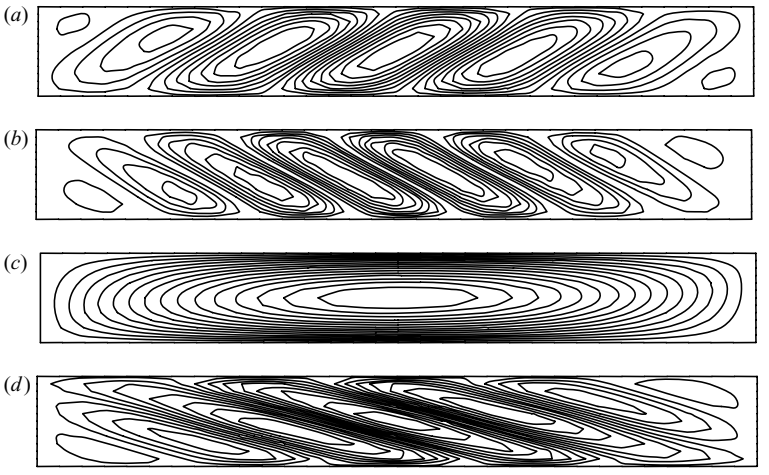


FIGURE 12. Streamlines at the onset of convection for a cavity ($A=8$) for $\varphi=-1$; $a=10$: ($a$) heated from the bottom, ($b$) heated from the top; $a=1$: ($c$) heated from the bottom, ($d$) heated from the top.

constant $R^0$ tends asymptotically towards the value $|R^0|=106/a$ where $A_C \to 2.5$. Naturally, this result is independent of the heating mode (from below or from the top) imposed on the horizontal walls. Figure 12 presents the effect of side-heating coefficient $a$ on the streamline patterns at the onset of convection as predicted by the linear stability analysis for a shallow cavity with an aspect ratio $A=8$. Typical streamlines corresponding to large values of $a$ ($a=10$) are in figures 12($a$) and 12($b$), for the case of a layer heated from the bottom and from the top, respectively. The inclination of the cells is different because the direction of the horizontal temperature gradients is reversed for the two heating modes considered here. The influence of the Soret effect on the onset of motion in a tall vertical enclosure subject to constant heat fluxes has been investigated by Mamou, Vasseur & Bilgen (1998) for the case where the buoyancy forces induced by the thermal and solutal effects are opposing each other and of equal intensity. For this situation, both the streamlines patterns and the resulting critical Rayleigh number were found to be equivalent to the results obtained here for a horizontal layer. This is not surprising since it has been demonstrated by Mamou (1997) and Mamou *et al.* (1998) that in the case of the onset of double diffusive convection in a vertical or horizontal fluid layer subject to equal and opposite fluxes of heat and mass, the supercritical Rayleigh number for the onset of motion is given by $R_{TC}^{sup}(1-Le)=105.3$. Hence, the constant $R^0$ has the same value for the two problems. However, the dependence of $R_{TC}^{sup}$ on $Le$ is observed to be different. As the value of $a$ is made very small, i.e. when the vertical temperature and mass fraction gradients are predominant over the horizontal ones, figure 11 indicates that, as expected, $R^0$ depends strongly on the heating mode. Thus, when the cavity is heated from the top and cooled from the bottom, $A_C \to \infty$, resulting in a parallel flow pattern at the onset for which $R^0 \to 12$ (in agreement with (5.3), a constant reported by Nield (1967) for the case of a porous layer subject to constant fluxes of heat and mass (see for instance figure 12$c$ for $a=1$). On the other hand, when the cavity is heated from the bottom, figure 11 indicates that $|R^0|$ (i.e. $R_{TC}^{sup}$) $\to \infty$ as the value of $a \to 0$. Thus, according to the linear stability theory, the fluid layer becomes unconditionally stable for this situation since the buoyancy forces resulting from the stabilizing agent (mass) are predominant over those from the destabilizing one (heat), which is also in

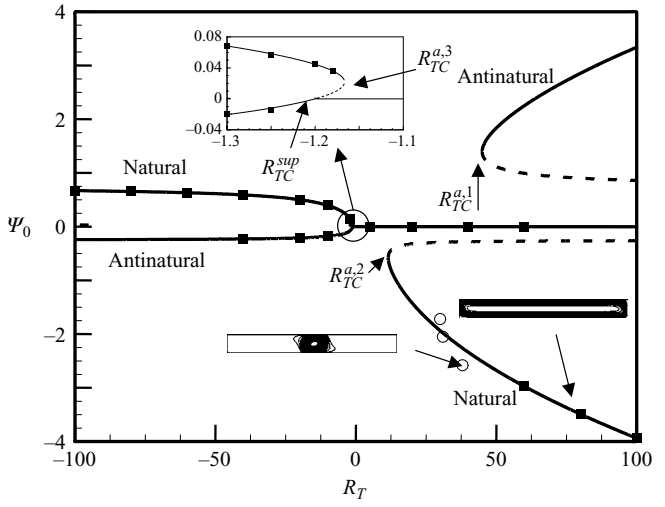


FIGURE 13. Bifurcation diagram as a function of $R_T$ for $\varphi = -1$, $Le = 10$ and $a = 0.3$: flow intensity $\Psi_0$. —, - - -, analytical; ■, numerical.

agreement with the parallel-flow approximation. Figure 12(*d*) shows the streamlines obtained for a cavity heated from the top, and for a relatively low value of $a$, namely $a = 1$.

5.2.2. *Finite-amplitude convection*

The results of the approximate analytical solution will now be considered for $\varphi = -1$, for which (4.15) becomes:

$$g(\Psi_0, R_T) = \Psi_0\left(Le^4\Psi_0^4 - 2bLe^2 d_1\Psi_0^2 - b^2 d_2\right) + d_3\Psi_0^2 + d_4 = 0, \tag{5.17}$$

where

$$\left.\begin{aligned} d_1 &= \bar{R}_T Le^2 - (Le^2 + 1), & d_2 &= -4\bar{R}_T Le^2 - 4Le^2, \\ d_3 &= \frac{3}{2}\bar{R}_T abLe[Le^3 - (1 - Le^2)], & d_4 &= -3\bar{R}_T ab^2 Le. \end{aligned}\right\} \tag{5.18}$$

Thus, $\Psi_0 = 0$ is always a solution of (5.17). Nevertheless, (5.17) predicts a supercritical Rayleigh number for the onset of convection: $R_{TC}^{sup,p} = 12/Le$, in agreement with (5.3).

The critical Rayleigh number predicted by the parallel-flow approximation ($A_C \to \infty$) is different from the supercritical Rayleigh number predicted by the linear stability analysis (for which $A_C$ is finite, as illustrated in figure 11). Thus, for the special case $\varphi = -1$, the present analysis yields six different Rayleigh numbers for the onset of convection, namely three subcritical Rayleigh numbers $R_{TC}^{a}$, one supercritical Rayleigh number predicted by the parallel-flow approximation $R_{TC}^{sup,p}$ and two supercritical Rayleigh numbers $R_{TC}^{sup}$ predicted by the linear stability theory.

Figure 13 shows the bifurcation diagram $\Psi_0$ versus $R_T$, obtained for $\varphi = -1$, $Le = 10$ and $a = 0.3$. In the absence of side heating ($a = 0$), the analytical solution (not presented here) shows that for $R_T < 0$, the onset of convection occurs through a pitchfork bifurcation at a supercritical Rayleigh number $R_{TC}^{sup} = -1.2$ as predicted by the linear stability theory and the parallel flow approximation (5.3). Naturally, the resulting unicellular convective pattern rotates indifferently clockwise or counter-clockwise. The imposition of side heating ($a \neq 0$) modifies the bifurcation diagram

described above in the way depicted in figure 13. For $R_T < 0$, the purely diffusive solution is stable down to $R_{TC}^{sup} = -1.2$ where it undergoes a transcritical bifurcation. From this point, two solution branches are observed to occur. The first solution ($R_T < -1.2$) is a stable supercritical branch corresponding to an 'antinatural' flow. Numerical confirmation of this solution was obtained down to $R_T = -45$, below which the resulting flows were found to be unstable and to evolve towards the more stable upper 'natural' convection curve. The second solution ($R_T > -1.2$) is the unstable subcritical solutal branch which undergoes a saddle-node bifurcation at $R_{TC}^{a,3} = -1.16$ and becomes stable, as demonstrated numerically. The effect of side heating for $R_T > 0$ will be now discussed. For this situation, the purely diffusive solution is stable up to $R_{TC}^{sup} = 516.06$, according to the linear stability theory. On the other hand, the present nonlinear analytical model shows that the effect of $a$ is to break the symmetry of the two subcritical branches obtained for $a = 0$ and for which the turning points are at $R_{TC}^{sub} = 22.87$. Thus, the turning point of the upper 'antinatural' branch ( $\Psi_0 > 0$) occurs now at $R_{TC}^{a,1} = 44.99$ whereas that of the lower natural branch ($\Psi_0 < 0$) occurs at $R_{TC}^{a,2} = 11.53$. It has not been possible to obtain a numerical confirmation of the upper curve for the range of Rayleigh numbers considered here. However, a good agreement between the analytical and the numerical results is observed for the natural branch for values of $R_T$ down to 55. At this particular Rayleigh number, it was found that not only are a unicellular parallel flow and a purely diffusive solution possible but, upon using appropriate initial conditions, a flow structure consisting of two corotating cells separated by a stagnant fluid is also predicted numerically. Upon further reducing the Rayleigh number, the numerical results indicate the existence, in the range $25 < R_T < 50$, of a flow structure consisting in a single cell located in the centre of the cavity, as already discussed in figure 10. For $R_T < 25$, the rest state is the only stable possible solution predicted by the numerical simulation.

The transcritical bifurcation described in figure 13 is characterized by the fact that the onset of convection occurs with an infinite wavenumber ($A_C \to \infty$) for which both the stability and the parallel-flow approximation yield the same supercritical Rayleigh number. This is not always the case as illustrated in figure 14 for $Le = 10$ and $a = 5$, according to the parallel-flow approximation, $R_{TC}^{sup,p} = -1.20$. However, from the linear stability analysis, the onset of motion occurs for $A_C = 4.79$, corresponding to $R_{TC}^{sup} = -1.16$. Thus, it is seen from figure 14 that the purely diffusive solution is stable down to $R_{TC}^{sup} = -1.16$. This point is connected, by an unstable branch, to $R_{TC}^{sup,p} = -1.20$ from which two solution branches are observed to occur, similarly to the case in figure 13. Numerical confirmation of the present theory was obtained for the upper curve ('natural' flow), but not for the lower curve ('antinatural' flow), at least for the range of $Ra$ considered in figure 14.

## 6. Conclusion

The role of the Soret effect in the natural convection within a shallow horizontal porous enclosure subjected to cross fluxes of heat was examined analytically and numerically. Results were obtained for a wide range of the governing parameters, namely the thermal Rayleigh number $R_T$, the separation parameter $\varphi$ , the Lewis number $Le$ and the constant $a$ controlling the fraction of the heat flux imposed on the vertical walls with respect to that imposed on the horizontal walls.

The linear stability theory was used to investigate the onset of supercritical convection for the special case $\varphi = -1$, for which the thermal and solutal buoyancy forces are opposing each other and of equal intensity. The results obtained both for

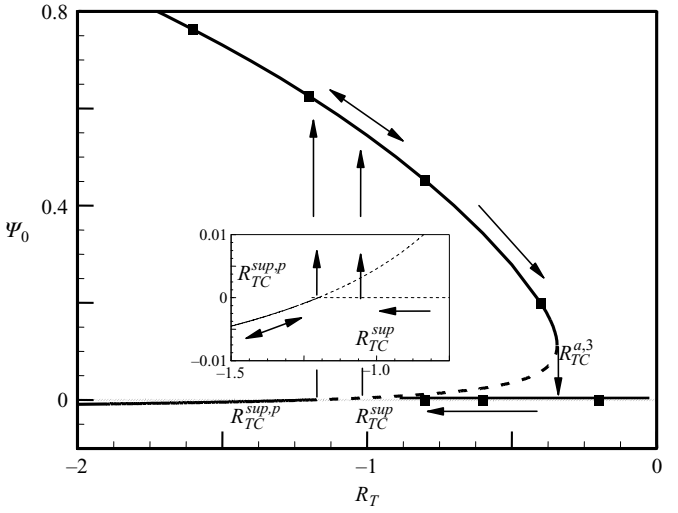


FIGURE 14. Bifurcation diagram as a function of $R_T$ for $\varphi = -1$, $Le = 10$ and $a = 5$: flow intensity $\Psi_0$. —, - - -, analytical; ■, numerical.

an infinite layer and a bounded cavity show that the physical problem has only one non-dimensionnal stability parameter $R_{TC}^{sup} Le = R^0$. The constant $R^0$, which depends upon the parameters $A$ and $a$, is, in fact, equivalent to that reported in the past for the case of double-diffusive convection (with the same thermal and solutal boundary conditions). However, for this last situation, the dimensionless group predicted by the linear stability analysis is given by $R_{TC}^{sup}(Le - 1) = R^0$.

The parallel-flow approximation was used to investigate the influence of the governing parameters on finite-amplitude convection within a shallow porous cavity ($A \gg 1$). In the absence of a horizontal gradient ($a = 0$), typical bifurcation diagrams have been obtained for both pure fluids and for binary fluids with the Soret effect. For $\varphi > 0$, i.e. when both thermal and solutal contributions are destabilizing, the threshold for the onset of convection occurs through zero flow amplitude (supercritical bifurcation), in agreement with the linear stability theory. The present theory shows that the supercritical Rayleigh number $R_{TC}^{sup}$, for the onset of finite-amplitude convection, depends on $\varphi$ and $Le$. As expected, the bifurcation thresholds for the binary fluid are below those for the pure fluid. However, for $\varphi < 0$, i.e. when a destabilizing thermal force is counteracted by a stabilizing solutal force, the threshold for the onset of convection occurs, in general, through finite flow amplitude (subcritical bifurcation).

The imperfection brought by side heating ($a \neq 0$) to the bifurcation curves was also investigated. For $\varphi > 0$, both the analytical and the numerical results indicate the existence of 'natural' and 'antinatural' flows. Numerically, the 'natural' flow can be obtained by starting the numerical procedure from pure conduction as the initial condition. By contrast, an impulsive flow pattern in the appropriate direction is required as an initial condition in order to reach the 'antinatural' state. This latter exists only if the Rayleigh number is above a subcritical Rayleigh number $R_{TC}^{a}$ which depends on $a$, $\varphi$ and $Le$. For $\varphi < 0$, the situation is more complex, and it is possible to obtain up to five different solutions (three stable and two unstable), for a given set of governing parameters. Two of the stable solutions correspond to 'natural' flows and the third one to an 'antinatural' flow. For the particular case $\varphi = -1$, it is demonstrated that steady bifurcations are either pitchfork or transcritical depending

on $a$, $Le$ and the sign of $R_T$ (i.e. on whether the cavity is heated from the top or from the bottom).

Numerical results show the existence of multiple steady states near the turning points, for a given range of the governing parameters. Some of these solutions were found to have a non-parallel flow structure.

## Appendix

The linear stability analysis reported in § 5.2 relies on the assumption that the instability in the $(x, y)$-plane is less stable than that in the $(x, z)$-plane. The validity of this assumption is now discussed.

For three-dimensional convection, the non-dimensional governing equations for the special case $\varphi = -1$, are given by

$$\frac{\partial u}{\partial x} + \frac{\partial v}{\partial y} + \frac{\partial w}{\partial z} = 0, \tag{A 1}$$

$$u = -\frac{\partial P}{\partial x}, \tag{A 2}$$

$$v = -\frac{\partial P}{\partial y} + R_T(T - C), \tag{A 3}$$

$$w = -\frac{\partial P}{\partial z}, \tag{A 4}$$

$$\frac{\partial T}{\partial t} + u\frac{\partial T}{\partial x} + v\frac{\partial T}{\partial y} + w\frac{\partial T}{\partial z} = \nabla^2 T, \tag{A 5}$$

$$\varepsilon\frac{\partial C}{\partial t} + u\frac{\partial C}{\partial x} + v\frac{\partial C}{\partial y} + w\frac{\partial C}{\partial z} = \frac{1}{Le}(\nabla^2 C - \nabla^2 T), \tag{A 6}$$

where $P$ and $w$ are the pressure and velocity component on the $z$-direction, respectively.

The linear stability of the rest state, for which $\boldsymbol{V}(u, v, w) = 0$ and $T = C = -ax - y$, is now investigated. Since the procedure is standard only the main steps are reported.

The solution of the perturbed equations of velocity, temperature and mass fraction is searched in normal modes, namely,

$$\left.\begin{aligned} \boldsymbol{V}(t, x, y, z) &= \boldsymbol{V}(y)\,\mathrm{e}^{pt+kx+lz}, \\ \Theta(t, x, y, z) &= \Theta(y)\,\mathrm{e}^{pt+kx+lz}, \\ \Phi(t, x, y, z) &= \Phi(y)\,\mathrm{e}^{pt+kx+lz}, \end{aligned}\right\} \tag{A 7}$$

where $k$ and $l$ are the wavenumbers in the $x$- and $z$-directions, respectively.

Upon substitution of (A 7) into the perturbed governing equations, the following set of linear equations are obtained:

$$\left(\frac{D^2}{k^2 + l^2} - 1\right)v + R_T(\Theta - \Phi) = 0, \tag{A 8}$$

$$p\Theta - (D^2 - k^2 - l^2)\Theta - \left[1 - ia\left(1 - \frac{l^2}{k(k^2 + l^2)}\right)D\right]v = 0, \tag{A 9}$$

$$p\Phi - \frac{1}{Le}(D^2 - k^2 - l^2)(\Phi - \Theta) - \left[1 - ia\left(1 - \frac{l^2}{k(k^2 + l^2)}\right)D\right]v = 0. \tag{A 10}$$

The above equations, together with homogeneous boundary conditions, may be written in a compact matrix form as:

$$\mathrm{L}(k, l)Y = p\mathrm{M}(k, l)Y, \tag{A 11}$$

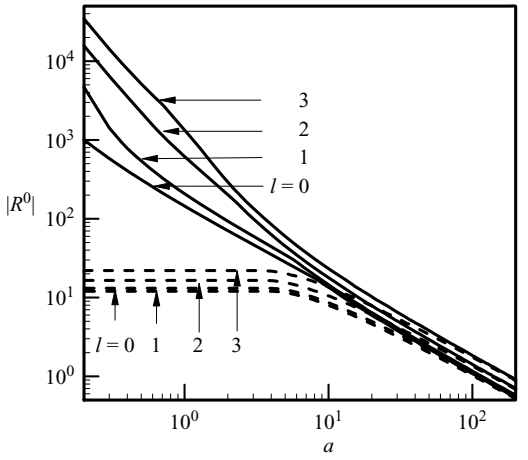


FIGURE 15. Effect of side heating coefficient $a$ and parameter $l$ on the constant $|R^0|$. —, heated from the top; - - -, heated from below.

where $Y$ is a three-component vector of the perturbations (velocity $v$, temperature $\Theta$ and mass fraction $\Phi$). $\mathrm{L}(k, l)$ and $\mathrm{M}(k, l)$ are two linear differential operators that depend on the control parameters ($Le$, $a$, $R_T$).

The system (A 11) was discretized, using a finite-difference scheme, in the domain between $y = 1/2$ and $y = -1/2$. With a standard subroutine for the eigenvalue problem (IMSL), the eigenvalue $p$ was obtained as a function of $Le$, $a$, $R_T$, $k$, $l$. Then, the supercritical Rayleigh number for the onset of motion $R_{TC}^{sup} = R^0(a, l)/Le$ was obtained and the results are presented in figure figure 15. The graph, in which $|R^0|$ is shown as a function of parameter $a$, clearly indicates that, for a cavity heated from below or from the top, the instability in the $(x, y)$-plane ($l = 0$) is less stable than in the $(x, z)$-plane ($l = 1, 2, 3 \ldots$). This result is found to independent of parameter $a$, the intensity of the side heating.

## REFERENCES


BAHLOUL, A., BOUTANA, N. & VASSEUR, P. 2003 Double-diffusive and Soret-induced convection in a shallow porous layer. *J. Fluid Mech.* **491**, 325–352.

BATISTE, O., ALONSO, A. & MERCADER, I. 2004 Hydrodynamic stability of binary mixtures in Bénard and thermogravitational cells. *J. Non-Equilib. Thermodyn.* **29**, 359–375.

BEJAN, A. & TIEN, C. L. 1978 Natural convection in a horizontal porous medium subjected to an end-to-end temperature difference. *J. Heat Mass Transfer* **100**, 191–198.

BERGEON, A., HENRY, D., BEN HADID, N. & TUCKERMAN, L.S. 1998 Marangoni convection in binary mixtures with Soret effect.*J. Fluid Mech.* **375**, 143–177.

BOURICH, M., HASNAOUI, M., AMAHMID, A. & MAMOU, M. 2002 Soret driven thermosolutal convection in a shallow porous enclosure. *Intl Commun. Heat Mass Transfer* **29**, 717–728.

BOURICH, M., HASNAOUI, M., MAMOU, M. & AMAHMID, A. 2004 Soret effect inducing subcritical and Hopf bifurcation in a shallow enclosure filled with a clear binary or a saturated porous medium: a comparative study. *Phys. Fluids* **16**, 551–569.

BOURICH, M., HASNAOUI, M., AMAHMID, A. & MAMOU, M. 2005 Onset of convection and finite amplitude flow due to Soret effect within a horizontal sparsely packed porous enclosure heated from below. *Intl J. Heat Fluid Flow* **26**, 513–525.

BRAND, H. R. & STEINBERG, V. 1983*a* Convective instabilities in binary mixtures in a porous medium. *Physica* **119**A, 327–338.

Brand, H. R. & Steinberg, V. 1983*b* Nonlinear effects in the convective instability of a binary mixture in a porous medium near threshold. *Phys. Lett.* **93** A, 333–336.

Chen, F. & Chen, C. F. 1993 Double diffusive fingering convection in a porous medium. *Intl J. Heat Mass Transfer* **36**, 793–807.

De Groot, S. R. & Mazur, P. 1962 *Non Equilibrium Thermodynamics*. North-Holland.

Kalla, L., Vasseur, P., Bennacer, R., Beji, H. & Duval, R. 2001 Double diffusive convection within a horizontal porous layer salted from the bottom and heated horizontally. *Intl Commun. Heat Mass Transfer* **28**, 1–10.

Kimura, S., Vynnycky, M. & Alavyoon, F. 1995 Unicellular natural circulation in a shallow horizontal porous layer heated from below by a constant flux. *J. Fluid Mech.* **294**, 231–257.

Mahidjiba, A., Mamou, M. & Vasseur, P. 2000 Onset of double-diffusive convection in a rectangular porous cavity subject to mixed boundary conditions. *Intl J. Heat Mass Transfer* **43**, 1505–1522.

Mamou, M. 1997 Convection thermosolutale dans des milieux poreux et fluides confinés. PhD thesis, Ecole Polytechnique of Montreal, Canada.

Mamou, M. & Vasseur, P. 1999 Thermosolutal bifurcation phenomena in porous enclosures subjected to vertical temperature and concentration gradients. *J. Fluid Mech.* **395**, 61–87.

Mamou, M., Vasseur, P. & Bilgen, E. 1998 Double diffusive convection instability problem in a vertical porous enclosure. *J. Fluid Mech.* **368**, 263–289.

Marcoux, M., Charrier-Mojtabi, M. C. & Bergeron, A. 1998 Naissance de la thermogravitation dans un mélange binaire imprégnant un milieu poreux. *Entropie* **214**, 31–36.

Nield, D. A. 1967 The thermohaline Rayleigh–Jeffreys problem. *J. Fluid Mech.* **29**, 545–558.

Ouarzazi, M. N. & Bois, P. A. 1994 Convective instability of a fluid mixture in a porous medium with time-dependent temperature. *Eur. J. Mech.* B/*Fluids* **13**, 275–298.

Patil, P. R. & Rudraiah, N. 1980 Linear convective stability and thermal diffusion of a horizontal quiescent layer of a two component fluid in a porous medium. *Intl J. Engng Sci.* **18**, 1055–1059.

Piquer, E., Charrier-Mojtabi, M. C., Azaiez, M. & Mojtabi, A. 2005 Convection mixte en fluide binaire avec effet Soret: étude analytique de la transition vers les releaux transversaux 2D. *C. R. Méc.* **333**, 179–186.

Platten, J. K. & Legros, J. C. 1984 *Convection in Liquids*. Springer.

Poulikakos, D. 1986 Double diffusive convection in a horizontal sparcelly packed porous layer. *Intl Commun. Heat Mass Transfer* **13**, 587–598.

Rosenberg, N. D. & Spera, F. G. 1992 Thermohaline convection in a porous medium heated from below. *Intl J. Heat Mass Transfer* **35**, 1261–1273.

Rudraiah, N., Shrimani, P. K. & Friedrich, R. 1982 Finite amplitude convection in a two-component fluid saturated porous layer. *Intl J. Heat Mass Transfer* **25**, 715–722.

Rudraiah, N., Shrimani, P. K. & Friedrich, R. 1986 Finite amplitude convection in a two-component fluid porous layer. *Intl Commun. Heat Mass Transfer* **3**, 587–598.

Sen, M., Vasseur, P. & Robillard, L. 1987 Multiple steady state for unicellular natural convection in an inclined porous layer. *Intl J. Heat Mass Transfer* **3**, 587–598.

Sovran, O., Charrier-Mojtabi, M. C. & Mojtabi, A. 2001 Naissance de la convection thermosolutale en couche poreuse infinie avec effet Soret. *C. R. Acad. Sci. Paris* **329** (11b), 287–293.

Taslim, M. E. & Narusaw, U. 1986 Binary fluid convection and double-diffusive convection in porous medium. *J. Heat Transfer* **108**, 221–224.

Taunton, J. W., Lightfoot, E. N. & Green, T. 1972 Thermohaline instability and salt fingers in a porous medium. *Phys. Fluids* **15**, 748–753.

Traore, P. & Mojtabi, A. 1994 Analyse de l'effet Soret en convection thermosolutale. *Entropie* **184/185**, 32–37.

Trevisan, O. V. & Bejan, A. 1987 Mass and heat transfer by high Rayleigh number convection in a porous medium heated from below. *Intl J. Heat Transfer* **30**, 2341–2356.